

RESEARCH ARTICLE | JULY 12 2023

A confocal laser-induced fluorescence diagnostic with an annular laser beam

I. Romadanov   ; Y. Raitses 



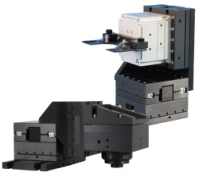
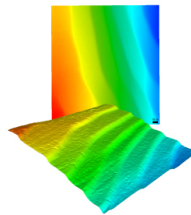
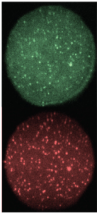


Rev Sci Instrum 94, 073002 (2023)

<https://doi.org/10.1063/5.0147669>



CrossMark

 <p>MCL MAD CITY LABS INC. www.madcitylabs.com</p>	<p>Nanopositioning Systems</p> 	<p>Modular Motion Control</p> 	<p>AFM and NSOM Instruments</p> 	<p>Single Molecule Microscopes</p> 
--	--	--	---	--

A confocal laser-induced fluorescence diagnostic with an annular laser beam

Cite as: Rev. Sci. Instrum. 94, 073002 (2023); doi: 10.1063/5.0147669

Submitted: 24 February 2023 • Accepted: 27 June 2023 •

Published Online: 12 July 2023



View Online



Export Citation



CrossMark

I. Romadanov^{a)}  and Y. Raites 

AFFILIATIONS

Princeton Plasma Physics Laboratory, Princeton, New Jersey 08543, USA

^{a)} Author to whom correspondence should be addressed: iromada2@pppl.gov

ABSTRACT

In this work, we report an annular beam confocal laser-induced fluorescence (LIF) configuration, which allows for high spatial resolution measurements of plasma properties in plasma setups and sources with limited optical access. The proposed LIF configuration utilizes the annular laser beam generated by a pair of diffractive axicons. The LIF signal is collected along the main optical axis within the ring region. It is shown experimentally that at a focal distance of 300 mm, a spatial resolution of ~ 5.3 mm can be achieved. Using geometric optics estimations, we showed that ~ 1 mm resolution at the same focal distance could potentially be achieved by modifying laser beam parameters. This approaches the localization accuracy of conventional LIF collection methods (with crossing laser beam injection and fluorescence collection optical paths). Measurements of the ion velocity distribution function in an argon plasma using both the confocal LIF with an annular laser beam and conventional LIF demonstrate a satisfactory agreement. The proposed LIF setup has potential applications for diagnostics in various plasma processing equipment and plasma sources, such as hollow cathodes, microplasmas, electric propulsion, etc.

Published under an exclusive license by AIP Publishing. <https://doi.org/10.1063/5.0147669>

I. INTRODUCTION

Laser-induced fluorescence (LIF) is a non-invasive, active optical diagnostic technique that is commonly used for measuring the velocity distribution function (VDF) of ions or neutral species in low-temperature plasmas in a range of conditions, from weakly collisional low-pressure plasmas to collisional plasmas generated at elevated pressures. The principle of the LIF diagnostic is based on the optical pumping of a plasma sample with a laser light and analyzing the resulting fluorescence signal. By using a narrow linewidth tunable laser, this diagnostic method is able to provide high-resolution information about the velocity distribution function of plasma species.¹ This makes LIF a versatile and valuable tool for plasma physicists and engineers studying plasma behavior in various applications. The VDF obtained from LIF can provide information about important parameters such as ion or atom temperatures and flow velocities. When the relation between the ground state and excited states is known, the absolute densities can be deduced from VDF data. In this paper, we focus on LIF measurements with excitation from metastable levels in weakly collisional plasma with non-equilibrium VDFs. Under such conditions, the measurements of the LIF signal, as the laser wavelength is scanned over a Doppler-

broadened transition, provide a profile of the VDF. This approach is commonly used for the measurements of VDFs for ions and atoms of numerous gases with applications to, for example, plasma thrusters, ion sources, and basic plasma science experiments such as plasma-wall interactions, double layers, etc.^{2–11}

The conventional LIF diagnostic requires optical access to plasma from the following two directions: one for the laser beam injection and another for the fluorescence emission collection.¹² In such configurations, spatial resolution is defined as an overlap between injection and collection focal regions. This overlap is minimized when an angle between the laser beam and the collection optical axis is 90° , resulting in sub mm spatial resolutions. However, this sets a limit on the applicability of this technique for some plasma sources, as it is not always possible or allowable to provide the required optical access (e.g., plasma hollow cathodes and anodes and plasma processing reactors for microelectronics). Several in-depth reviews of conventional LIF measurements with intersecting optical paths are available in the literature.^{13,14}

A confocal configuration of laser-induced diagnostics is widely used in biology and medicine,^{15–17} and there are several works demonstrating its application for Raman spectroscopy,^{18,19} Thompson scattering,²⁰ and for laser-induced fluorescence diagnostic.^{21,22}

The primary advantage of confocal configurations is the coincidence of the laser beam injection and fluorescence collection branches, enabling measurements in systems with limited optical access or complex geometries (e.g., industrial plasma sources used for microelectronics production, Hall thrusters, and magnetic fusion devices, etc.), where conventional LIF methods with intersecting injection and collection optical paths are not feasible. However, the spatial resolution of a confocal system is mainly defined by the depth of field (DOF) of the focusing/collection optics, which becomes challenging to maintain at smaller values as the distance to the measurement point increases. The DOF for the Gaussian beam can be expressed as

$$DOF = \frac{8\lambda}{\pi} \left(\frac{F}{D} \right)^2, \quad (1)$$

where λ is the wavelength, F is the focal length of the lens, and D is the lens diameter. To achieve high spatial localization, large diameter laser beams and optical elements are required for very long focal lengths. Despite the advantage of a single optical path in confocal LIF, its application can be limited by the need for high spatial localization and constraints on sampling volume.

A confocal optical arrangement was employed for two-photon LIF (TALIF). The spatial resolution was determined by the DOF of the optical setup. This is due to the TALIF intensity being proportional to the squared laser beam intensity. Consequently, contributions from fluorescence light outside of the focal region are significantly reduced. As a result, measurements were primarily concentrated within the DOF, leading to improved spatial resolution. In the works,^{22,23} a coaxial TALIF system was designed where the collection lens has an aperture at the center, which is used for passing the laser beam. The fluorescence signal is collected from the hollow cone, the base of which is defined by the difference between the lens and aperture diameters. The reported spatial resolution was about 20 mm at $f = 820$ mm focal distance. In more recent works,²⁴ the conservative estimation for TALIF measurements resolution of 5 mm was reported.

For single-photon LIF, the fluorescence intensity is directly proportional to the laser beam intensity; thus, spatial resolution is solely defined by the DOF of the optical setup. In a number of previous studies,^{25,26} there were attempts to overcome this issue, especially for setups with long focal distances. In Ref. 21, a spatial resolution of 3 cm at 20 cm focal length was achieved by using the fact that DOF is inversely proportional to the focused laser beam diameter. The laser beam was expanded in a beam expander and then focused with a 5 cm lens. In Ref. 25, the confocal design included the obstruction disk, which cuts the fluorescence light along the optical axis. The spatial resolution is then defined by the overlapping region between the hollow fluorescence cone and the laser beam. The reported resolution was about 1.4 mm at $f = 150$ and ~ 7.3 mm at $f = 500$ mm focal distance.²⁶ In a more recent work,²⁷ a spatial resolution of 1 mm was reported.

In all the above LIF configurations, the laser beam remains the same cylindrical shape, and the spatial resolution was ensured either by expanding the laser beam or by cutting the fluorescence light along the laser beam, thus reducing the overlap between the injection and collection paths. Although in the case of the expanded beam, when the collected fluorescence light was not cut, the achievable spatial resolution is moderate. Cutting the fluorescence light along the

optical axis would result in a reduction of the signal-to-noise ratio (SNR), which can be crucial for the cases of low plasma density or bright emitting background within the field of view (e.g., thermionic cathode).

Here, we present a proof-of-concept LIF configuration with an annular laser beam, which ensures a relatively high spatial localization of a few mm over large focal distances of >200 mm with a high SNR (>10). The large diameter annular laser beam (22 mm) ensures a small DOF. All fluorescence light enclosed by the focused laser beam is collected, resulting in a high SNR. A set of diffractive axicon lenses was used to create an annular laser beam of high quality. With the current setup, the achieved spatial resolution is 5.3 mm at $f = 500$ mm focal distance. Here, the spatial resolution is defined as a region with 95% of focused laser beam intensity. The paper is organized as follows: the experimental setup and LIF diagnostics used in this work are described in Secs. II and III, respectively; and the measurement results are presented and discussed in Sec. IV, followed by conclusions in Sec. V.

II. EXPERIMENTAL SETUP

The reported experiments were performed with an argon plasma generated by a 100 W DC discharge with a thermionic cathode in a fully enclosed container with an approximate volume of 10^5 mm³ (see Fig. 1). The source is installed in a vacuum chamber made from a standard 10 in. diameter six-way cross. The chamber is equipped with mechanical and turbomolecular pumps. The source has a 1 cm diameter opening on the longer front wall (Fig. 1). This opening allows vacuum pumping of the gas from the source and access for diagnostics of the enclosed plasma (e.g., by probes, optical emission spectroscopy, and laser diagnostics). In the described experiments, the argon background gas pressure measured with a commercial ion gauge in the vacuum chamber was in the 100 μ Torr range, whereas the argon gas pressure in the source was estimated to be about ten times higher. Under such conditions, plasma in the source is weakly collisional with the ion mean-free path, $\frac{\lambda_i}{L} \gg 1$, whereas plasma leaking through the opening is nearly collisionless. Here, L is the width of the source in z -direction.

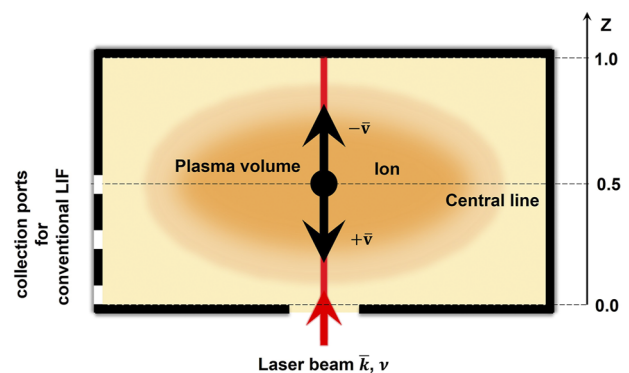


FIG. 1. Schematic of the plasma source (not to scale) showing enclosed plasma volume with a diagnostic opening of about 10 mm diameter at the front side and three collection ports of 3 mm diameter each on the side, which was used for the conventional LIF. Confocal LIF collection points were evenly spaced between $Z = 0.0$ and $Z = 0.5$ (dimensionless locations).

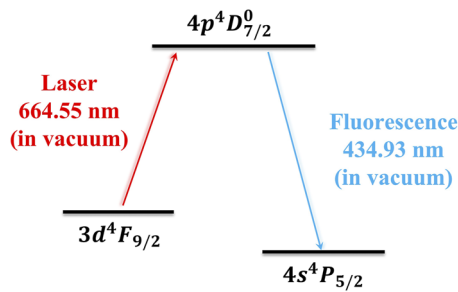


FIG. 2. LIF transition for Ar-II (argon ion).

For the implementation of the confocal and conventional LIF configurations, the laser beam with the wavevector \mathbf{k} and frequency ν is injected through the 10 mm opening on the front wall. In addition, for the conventional LIF, the source has three additional 3 mm diameter orifices on its side wall. These orifices are used to collect the LIF signal from the three spatial locations ($Z = 0.0$ to $Z = 1.0$) as shown in Fig. 1 (note that z is in the same direction here as will be shown in Figs. 4 and 5).

In this work, LIF measurements are performed by sweeping the frequency of a tunable diode laser with a narrow linewidth over the absorption line of an argon ion that is broadened due to Doppler shift. By measuring the emission intensity at different laser wavelengths, a VDF profile can be recovered. For an argon ion, a three-state scheme is used. The selected transition is illustrated in Fig. 2.

Ar ion at the $3d^4F_{9/2}$ metastable state is optically pumped by a 664.553 nm (in vacuum) laser light to the $4p^4D_{7/2}$ state, which decays to the $4s^4P_{5/2}$ state by emission at 434.929 nm.^{28,29} This transition was chosen over more commonly used $3d^4F_{7/2} - 4p^4D_{5/2}$ (excitation at 668.614 nm and emission at 442.724 nm)³⁰ as having better signal intensity for the experimental conditions. Plasma ion density profiles along the z -axis were measured with a cylindrical, tungsten Langmuir probe (diameter $d_p = 0.1$ mm and length

3 mm), negatively biased at -40 V and installed on a moveable stage. Plasma density was obtained from the orbital motion limited (OML) theory.³¹ Probe measurements were conducted through the same 10 mm diagnostic opening utilized for LIF measurements. Measurements were carried out along the direction of the laser beam path. A distance increment of 2 mm was set. These profiles were used to compare with metastable density profiles obtained from VDF data.

III. CONFOCAL LIF SETUP WITH ANNULAR LASER BEAM

A. Annular beam generation with axicons

Axicon is an optical element, which allows for annular beam formation.³² The principle of the operation of the refractive axicon is shown in Fig. 3(a). Due to the conical shape of the axicon, the passing laser beam with a diameter 2δ is transformed into the annular beam with the annulus thickness of $\approx \delta$. Such beams can be collimated with the second axicon of the same geometry. The diameter of the collimated beam is determined by the distance between two axicons.

Refractive axicons,³³ as shown in Fig. 3(b), suffer from beam interference due to imperfect geometry of the optical element. This results in the formation of the region with the residual intensity within the laser light ring (see Ref. 6 for more details). This will result in a reduction of the spatial resolution, due to the increased focal spot size.

In this work, a pair of diffractive axicons (DA), which were custom made by HOLO/OR for 670 nm wavelength, was used.³⁴ The element size is 25.4 mm, with a clear aperture of 22.9 mm and an equivalent apex angle of 170° . Diffractive axicon results in very low residual intensities of the central region, as shown in Fig. 3(c). The quality of the annular beam is sensitive to the input beam shape and beam collimation. To improve the performance of the DA element, the laser beam was converted into a circular beam of 3 mm in diameter with a Gaussian intensity profile by fiber coupling and follow-up collimation (see Sec. III C).

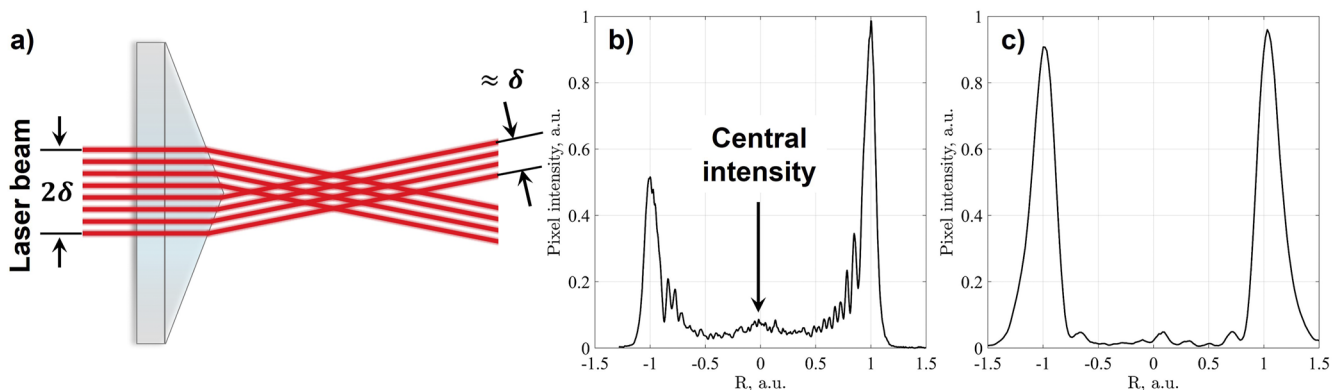


FIG. 3. (a): Conventional axicon and annular beam generation (see Ref. 5 for more details), (b) annular beam profile after refractive axicon (R is normalized to 2 mm), and (c) annular beam profile after the DA (R is normalized to 2 mm). The input Gaussian beam diameter was maintained at 3 mm for all measurements. The beam profile was measured ~ 200 mm away from the axicon, after focusing it with an $f = 100$ mm lens to fit it onto the camera sensor.

B. Annular beam confocal (ABC)-LIF setup

The LIF system is built around a single-mode TOptica DLC DL PRO 670 tunable diode laser (TDL), and its design is shown in Fig. 4. The diode laser is a Littrow-type grating stabilized external cavity design and has a coarse tuning range between 660 and 673 nm and a mode-hop free tuning range of 20 GHz. The output power is wavelength-dependent, with a maximum value of about 23 mW. Power variations during the wavelength scan were monitored with a wavemeter and were found to be below 10% over the scan range. The LIF signal was corrected by multiplying lock-in values by the value of the normalized power at each laser frequency. The short-term linewidth stability is 600 kHz (over 5 μ s). The laser wavelength is controlled by scanning the voltage applied to the piezo actuator. The output beam is a Gaussian beam of elliptical shape with a characteristic size of about 3 mm.

Part of the laser beam is sampled by a beam splitter (BS1) and is directed to the Bristol 621-A wavemeter, which has a built-in continuous calibration (single-frequency He-Ne laser, accuracy ± 0.0002 nm at 1000 nm). With this accuracy, the achievable velocity resolution is ~ 60 m/s. The main beam is modulated by the mechanical chopper (C1), which is set to a frequency of 2 kHz. The modulated beam is sampled with the beam splitter (BS2), and the sampled beam is set to the photodiode (PD). The output of the photodiode provides the reference frequency for the lock-in amplifier.

The beam is then directed by the mirror M1 through the fiber launch system (FLS) Thorlabs MBT613D into a single-mode fiber. This is to ensure the circular beam shape with a Gaussian profile. The fiber output was collimated with a F260FC-B collimator providing a 3 mm diameter beam.

The beam is then passed through a pair of diffractive axicon lenses (DA1, 2-HOLO/OR 670 nm), which are installed in XY adjustable mounts to ensure their coaxiality. Both diffractive axicons are installed on the rotation (around the Y axis) stages to ensure that they are parallel to each other. The beam quality after the axicons was verified with the CMOS camera. Circularity, equal intensity

distribution, and the absence of light intensity within the ring were monitored. After the axicons, an annular beam (with a diameter of ~ 22 mm) is directed by mirror M2 and dichroic mirror D1 (short-pass, 490 nm cutoff) into the vacuum chamber. Beam focusing is achieved by lens L1 with the focal distance $f = 300$ mm.

The fluorescence light is collected by the same lens L1 and then passed through the dichroic mirror D1. Iris I1, which has an inner diameter of 19 mm, selectively cuts the outer part of the collimated light cylinder. This serves to reduce the contribution of fluorescent light from species that are excited along the laser beam path, rather than solely at the focal spot. By doing so, Iris I1 helps maintain the system's spatial resolution by minimizing the influence of fluorescence that occurs outside the focal spot. The collected light is then passed through the bandpass filter 430/10 nm (Thorlabs FBH430-10) and then focused by lens L2 with the focal distance $f = 50$ mm into the 100 μ m pinhole P1. The pinhole mainly eliminates stray light from the dichroic mirror and other optical elements, with its diameter being large enough to not influence the DOF. After the pinhole, the light is sent into the photomultiplier tube (PMT). The PMT output is fed into the lock-in amplifier input, and the fundamental component, arising due to laser beam amplitude modulation, is filtered out. Laser wavelength and readings from wavemeter and lock-in amplifier outputs (signal and phase) are collected with in-house-developed LabVIEW-based software.

The fluorescence excitation line shape can broaden if the transition is saturated due to high laser intensity.³⁵ LIF signal intensity was measured as a function of the laser power to ensure such line-shaped distortions are prevented. A linear relation between fluorescence signal and laser power was observed, confirming that the measurements were conducted within the unsaturated regime.

C. Conventional LIF setup

A diagram of the conventional optical arrangement used in these experiments is presented in Fig. 5. The laser, wavemeter, and data acquisition electronics were maintained the same as in the

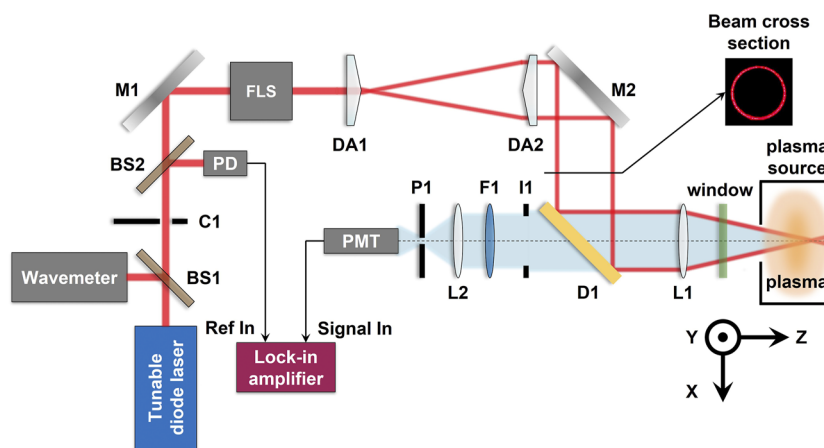


FIG. 4. Block diagram of the ABC-LIF setup and beam path into the ion source. BS—beam splitter; C—mechanical chopper, PD—photodiode; M—mirror; FLS—fiber launch system; DA—diffractive axicon; L—lens; D—dichroic mirror; I—iris; F—bandpass filter; P—pinhole; and PMT—photomultiplier tube.

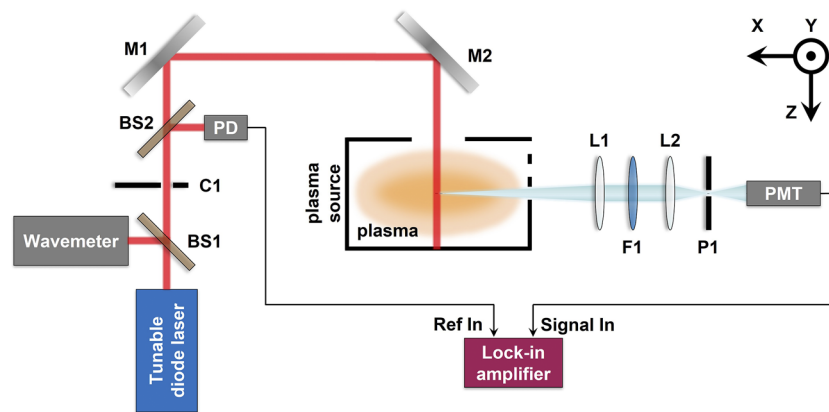


FIG. 5. Block diagram of the conventional LIF setup and beam path into the ion source. BS—beam splitter; C—mechanical chopper, PD—photodiode; M—mirror; L—lens; I—iris; F—bandpass filter; P—pinhole; and PMT—Photomultiplier tube.

confocal setup. The beam path into the chamber is similar to the confocal setup, except that no axicons were installed, and the beam was directed into the chamber immediately after mirror M2. The beam was not focused before entering the chamber to simplify the alignment between the injection and collection paths by increasing the emission volume created by the laser beam. Measurements were performed through three collection ports on the side of the plasma source, which were specifically designed for LIF measurements and are not part of the original design. The port diameter is ~ 3 mm. Light collected with lens L1 with $f = 400$ mm, passed through the bandpass filter F1–430/10 nm (Thorlabs FBH430-10) and then focused by lens L2 with a 50 mm focal length into the $100 \mu\text{m}$ pinhole P1. Light collection was performed with a PMT, and the output was fed into a lock-in amplifier. The collection path was installed on a translational stage along the z to avoid realignment for each diagnostic hole. The spatial resolution of this system was determined by the pinhole diameter d_{pinhole} multiplied by f_{L1}/f_{L2} that is 0.8 mm.

D. Light collection and spatial resolution in the confocal setup with the annular beam

Light collection with the proposed confocal setup is illustrated in Fig. 6. The collimated annular laser beam is focused with lens L . Fluorescence intensity is maximized in the region with maximum laser intensity at the focal distance f . Fluorescence light, spreading in all directions from the focal point, is collected with the same lens L , forming a light cone with base L and height f [shown in blue in Fig. 6(b), not to scale]. The base of this cone can be reduced, avoiding overlap with the laser beam path. From this sketch, one can see that the spatial resolution is defined only by the overlap volume between the laser beam and collection cones. The contour of the overlap area is marked with black lines. However, due to nonuniform laser intensity distribution, only fluorescence light from the shaded area is the main contributor to the detected signal.

Spatial resolution or DOF is defined by the intersection between annular beam paths at the focal point. This is illustrated in Fig. 7(b), where the annular beam of radius R and annulus thickness δ are

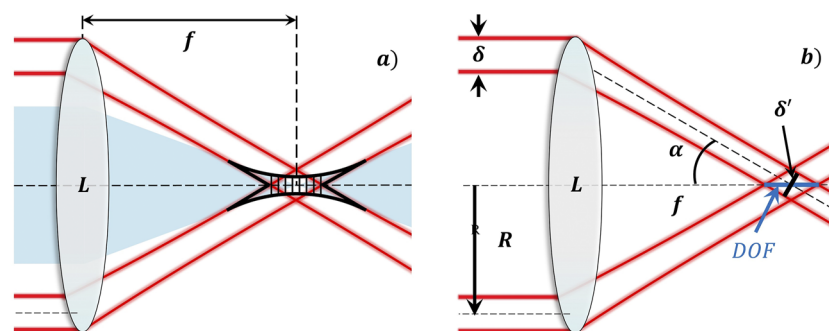


FIG. 6. (a) Fluorescence light collection with the proposed confocal design. L is a lens with a focal distance of f . Red lines mark the contour of the annular laser beam, and the blue region is the collected cone of the fluorescence light. The black line is the intersection of the fluorescence light cone, and the laser beam hollow cone. Black-shaded area is the collection volume. (b) Diagram showing DOF for the annular beam. R is the annular beam radius; δ is the annulus thickness; δ' is the beam waist at the focal plane; and DOF is the depth of focus.

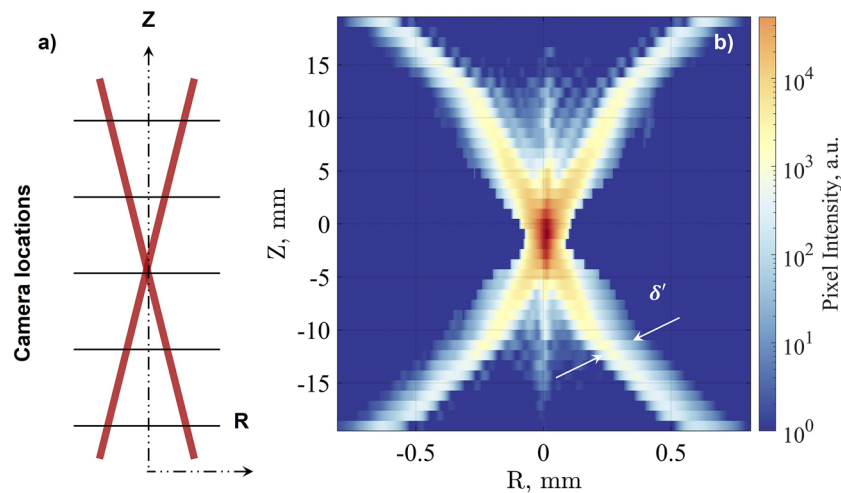


FIG. 7. Spatial resolution characterization. (a) Schematic of the experiment for spatial resolution characterization. (b) Cross-section of the beam profile, where δ' is the beam thickness at the lens focal plane.

focused by the lens with a focal length of f . From geometrical considerations, the length of DOF can be found as

$$DOF = \frac{4\lambda f}{\pi\delta} \frac{1}{\sin(a \tan(R/f))}, \quad (2)$$

where λ is the laser wavelength [see Eq. (4) in Ref. 36]. For the setup used in this work, $R \approx 11$ mm, $\delta = 1.5$ mm, $f = 300$ mm, $\lambda = 668$ nm, and the theoretical DOF is ~ 4.6 mm. Note that this is an upper limit due to the laser intensity being not uniformly distributed (Gaussian) along the DOF. Such nonuniformity will result in smaller effective spatial resolution. It is important to note that the presented model is simplified and does not consider the hyperbolic shape of the focused laser beam. Additionally, the model does not account for the effect of the full volume of the overlap between the injection and collection paths (see Fig. 6), which contributes to a reduction in spatial resolution. The effect of optical aberrations, including geometrical and chromatic aberrations, can significantly influence spatial resolution, particularly at increased focal distances. However, these aberrations were not considered in the current model. Addressing and incorporating the impact of optical aberrations into the model will be a subject for future work to further refine the technique.

From Eq. (2), one can see that at a fixed focal length f , the DOF can be minimized by increasing δ or annulus radius R . For example, for an annular beam with $R = 20$ mm and $\delta = 3$ mm, it should be possible to achieve ~ 1 mm resolution. In the current setup, the main limit for the spatial resolution improvement is the axions diameter, which is 25.4 mm each, and the clear aperture is about 22 mm. By utilizing 2 in. optics (with clear aperture of ~ 48 mm) and further increasing the annulus thickness δ to 4 mm (with commercially available fiber collimators), it is possible to achieve a spatial resolution of 0.8 mm at $f = 300$ mm.

As demonstrated by Eq. (1) for Gaussian beams and Eq. (2) for ring-shaped beams, the DOF is inversely proportional to the incident beam area entering the focusing lens. The DOF of the proposed

setup is equivalent to that of a setup with a Gaussian beam having a radius of ~ 10 mm. However, the advantage lies in not overlapping the LIF signal while maintaining the DOF of an expanded beam.

The control of overlap volume in the proposed setup can be achieved by adjusting the annulus thickness δ and annulus radius R . This allows for the collection of all fluorescence light within the laser beam cone without compromising spatial resolution. The primary distinction between the current setup and the configurations presented in Refs. 25 and 26 lies in the improved control of spatial resolution. In Refs. 25 and 26, the obstruction disk determines spatial resolution, and achieving higher spatial resolution necessitates reducing collected fluorescence light, consequently leading to a decrease in SNR.

E. Spatial resolution characterization

To experimentally characterize the spatial resolution and the optical response function of our system, the CMOS camera on the movable stage was installed at the focal point of the lens L1 (see Fig. 4). The schematic of the experiment is shown in Fig. 7(a). The camera was moved along the optical axis (Z), and the beam profile images were collected. The origin was selected at the lens focal point. Camera exposure was adjusted at each position to avoid pixel saturation. Linearity of the camera pixel response to exposure time and laser intensity was verified. During post-processing, the image intensities at each location were corrected by applying a scaling factor $\tau_{\text{exp}}^N / \tau_{\text{exp}}^1$, where τ_{exp}^1 represents the exposure time at the first location, and τ_{exp}^N denotes the exposure at the current location N . The linearity of the camera's pixel response to both exposure time and laser intensity was confirmed. This correction procedure facilitated the relative comparison between different images captured with varying exposure times. All images were stacked together allowing for the laser beam profile visualization [see Fig. 7(b)].

Spatial resolution and optical response function were determined from the intensity profiles along the centerline at $R = 0$ mm,

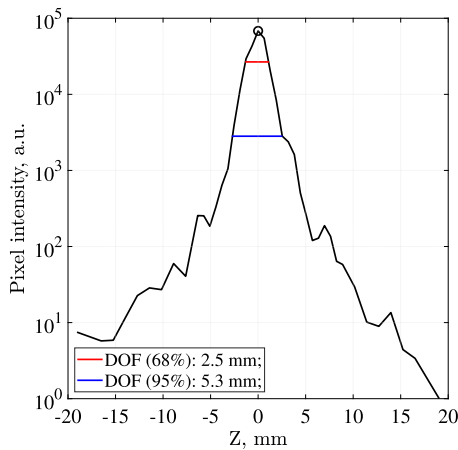


FIG. 8. Confocal optics response function, with defined DOF lines. The blue line corresponds to a region with 95% intensity, and the red line corresponds to a region with 68% intensity.

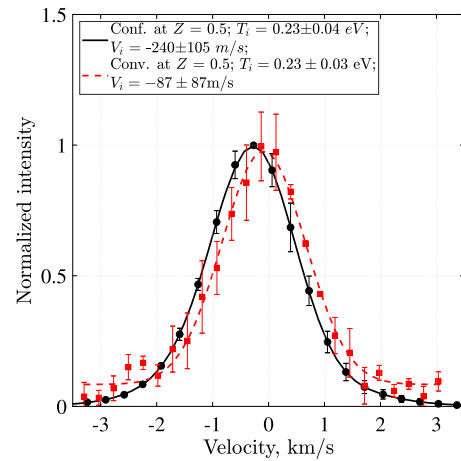


FIG. 9. Argon IVDF at $Z = 0.5$ obtained with conventional (red, squares) and confocal (black, circles) LIF setups.

which is shown in Fig. 8. The resolution was defined, conservatively, as a region that contains 95% of the laser beam intensity (blue line in Fig. 8). Experimentally found a value of 5.3 mm is close to the theoretical value of 4.6 mm obtained from Eq. (2). Resolution of the conventional method is about 0.8 mm. If the spatial resolution is defined as a region where only 68% of the laser beam intensity is contained, then the resolution of the confocal method is 2.5 mm (red line in Fig. 8).

IV. RESULTS

Measurements of the ion VDF (IVDF) were conducted along the beam path (in the z direction) at eight locations across several centimeters, with a focal distance of 300 mm. The focusing optics were installed on a translational stage with a micrometer, allowing for precise location control. The equation used to establish the relationship between the laser frequency offset and the velocity for both conventional and confocal schemes is as follows:

$$\frac{\Delta\nu}{\nu_0} = -\frac{\mathbf{v}}{c} \cdot \mathbf{k}, \quad (3)$$

where ν_0 represents the photon frequency, $\Delta\nu$ is the shift in photon frequency from the perspective of the particle, \mathbf{v} is the particle velocity, c is the speed of light, and \mathbf{k} is the photon wavevector. This relation holds for both conventional and confocal schemes. For the coordinate systems shown in Figs. 5 and 6, \mathbf{k} is along the z direction.

The typical IVDF profile obtained with confocal and conventional LIF setups at $Z = 0.5$ is shown in Fig. 9. Both signals are normalized to maximum intensity. The signal-to-noise ratio was defined as $SNR = \mu_{signal}/\sigma_{signal}$, where μ_{signal} is an average signal value and σ_{signal} is the noise standard deviation found after subtraction of the fitted function from the signal. For both methods, the obtained SNR values are $SNR = 7$ and $SNR = 90$ for conventional and

confocal setups, respectively. Ion temperatures and mean velocities were determined by fitting the IVDF profiles with

$$f(v) = \left(\frac{M_i}{2\pi k_B T_i} \right)^{1/2} e^{-\frac{M_i(v-v_0)^2}{2k_B T_i}}, \quad (4)$$

where M_i is ion mass, k_B is Boltzmann constant, T_i is ion temperature, and v_0 is the mean velocity. Error bars for ion temperature are defined as a standard deviation between three measurements. For ion velocity, error bars are a combination of a standard deviation of three measurements and wavemeter uncertainty, which is ~ 60 m/s. Both methods yield similar VDF shapes and close values for mean velocities and ion temperatures. The shift between VDFs (~ 0.1 km/s for the maximum LIF signal) can be attributed to the nonlocality of confocal measurements. In this context, nonlocality refers to the long DOF, causing the resulting VDF to be a weighted sum of all VDFs along the DOF. This differs from conventional LIF measurements, where VDFs represent a smaller DOF with constant density and laser power. The examined case, with measurements performed at the $Z = 0.5$ location, demonstrates that confocal LIF can be effectively implemented only in systems where the characteristic scale of the gradient of the quantity directly affecting the VDF signal strength, such as the density gradient, is larger than the DOF of the optical system.

Mean ion velocities and ion temperatures along the Z direction were compared with conventional LIF measurements performed at 3 positions, which are shown in Fig. 1. The results are shown in Fig. 10. One can see that the overall flow velocities between the two methods agree with the uncertainty. Ion temperature measurements show good agreement as well. General trends for both quantities are similar between confocal and conventional LIF measurements.

Integration of ion VDF obtained at different spatial locations will yield the metastable ion density profile. This profile was compared with ion density profiles measured with the biased Langmuir

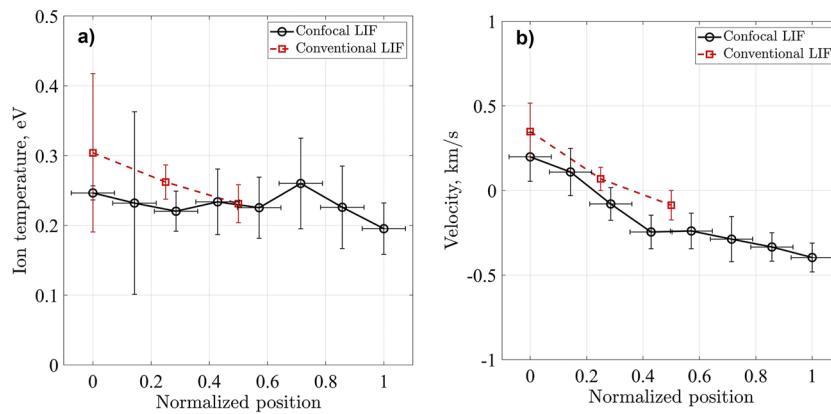


FIG. 10. Comparison of ion velocity (a) and ion temperature (b) distributions along the radial position obtained with conventional (dashed line) and confocal (solid) LIF setups. Vertical error bars are standard deviations from three repeated measurements. Horizontal error bars correspond to spatial resolution defined in Fig. 8.

probe along the beam path. Normalized profiles are shown in Fig. 11. As one can see, the LIF profile (black circles) is wider than the density profile obtained with the probe measurements (red squares). This is due to the nonlocality of the confocal measurements and differences between metastable ion density and total ion density measured by the probe. The effect of nonlocality can be eliminated if the optics response function is known (shown in Fig. 8). The reconstructed profile, obtained as a deconvolution of the LIF profile with the normalized optics response function, is shown as a black dashed line in Fig. 11. Deconvolution is performed with a custom MATLAB function.³⁷ It can be seen that the reconstructed profile closely follows the one measured with the probe.

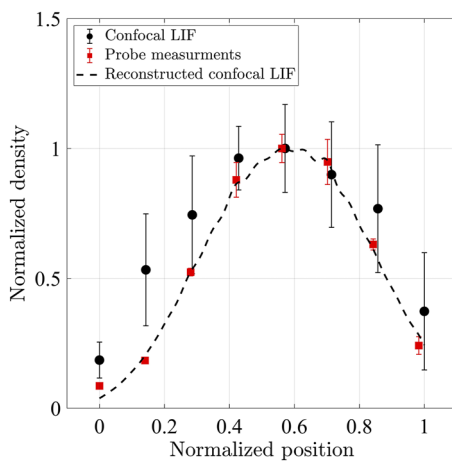


FIG. 11. Comparison of metastable density profile obtained with the confocal LIF (black circles) with the ion density measurements obtained with the biased Langmuir probe (red squares). The black-dashed line shows the density profile reconstructed from the deconvolution of the confocal LIF profile with the optical response function (Fig. 8). Error bars are standard deviations from three repeated measurements.

V. CONCLUSION

In this paper, the confocal LIF configuration based on an annular laser beam was introduced and characterized both with and without plasma. The key element of this setup is the diffractive axicon optics, which ensures high annular beam quality, essential for achieving high spatial localization. The spatial resolution of the current setup is 5.3 mm, which is comparable with other reported confocal schemes at similar focal distances.^{25,26} However, the proposed design offers several advantages.

First, the spatial resolution is controlled by the following laser beam parameters: annulus thickness and beam diameter. Our calculations indicate the potential to achieve a 1 mm resolution at the same focal distance by adjusting annular beam parameters. The proposed optical setup takes advantage of a reduced DOF through an increased beam diameter and the employment of an annular beam. This arrangement enables a spatial separation of laser light and signal, eliminating the need to decrease the collected fluorescent light for improved spatial resolution. As a result, the SNR in the suggested LIF configuration is maximized. Finally, this LIF configuration avoids problems with beam back reflection, as the reflected beam from the back wall (if present) will diverge out of the field of view.

In plasma experiments, the proposed LIF configuration was utilized for the measurements of argon ion VDF in an enclosed DC plasma source with limited optical access. A comparison of the confocal and conventional LIF showed good agreement between determined plasma parameters (ion temperature and flow velocities). Ion temperature, found with conventional LIF, varied from 0.30 ± 0.11 to 0.2 ± 0.03 eV between $Z = 0$ and 0.5. ABC-LIF showed changes in ion temperature from 0.25 ± 0.02 to 0.22 ± 0.05 eV for the same range. Measurements of flow velocities with the conventional method showed a velocity change from 350 ± 168 to -90 ± 87 m/s in $Z = 0-0.5$. Corresponding flow velocity changes determined with confocal LIF were from 200 ± 155 to -240 ± 100 m/s for the same range. Reconstructed metastable density profiles extracted from LIF spectra were compared with the Langmuir probe ion density measurements. It was shown that density profiles show satisfactory

agreement, which serves as a verification of the determined spatial resolution.

ACKNOWLEDGMENTS

This work was performed under the U.S. Department of Energy through Contract No. DE-AC02-09CH11466. Authors would like to acknowledge Dr. S. Kondeti and Dr. S. Yatom for discussions and their help with the setup.

AUTHOR DECLARATIONS

Conflict of Interest

The authors have no conflicts to disclose.

Author Contributions

I.R. and Y.R. contributed equally to this work.

I. Romadanov: Conceptualization (equal); Funding acquisition (equal); Methodology (equal); Resources (equal); Visualization (equal); Writing – original draft (equal); Writing – review & editing (equal). **Y. Raitses:** Conceptualization (equal); Investigation (equal); Project administration (equal); Resources (equal); Supervision (equal); Writing – original draft (equal); Writing – review & editing (equal).

DATA AVAILABILITY

The data that support the findings of this study are available from the corresponding author upon reasonable request.

REFERENCES

- ¹R. A. Stern and J. A. Johnson, *Phys. Rev. Lett.* **34**, 1548 (1975).
- ²R. Spektor, K. D. Diamant, E. J. Beiting, Y. Raitses, and N. J. Fisch, *Phys. Plasmas* **17**, 093502 (2010).
- ³N. Britun, T. Minea, S. Konstantinidis, and R. Snyders, *J. Phys. D: Appl. Phys.* **47**, 224001 (2014).
- ⁴R. S. Marshall and P. M. Bellan, *Rev. Sci. Instrum.* **91**, 063504 (2020).
- ⁵J. Carr, Jr., “Laser induced fluorescence studies of electrostatic double layers in an expanding helicon plasma,” Ph.D. thesis, West Virginia University Libraries, 2013.
- ⁶D. Kuwahara, Y. Tanida, M. Watanabe, N. Teshigahara, Y. Yamagata, and S. Shinohara, *Plasma Fusion Res.* **10**, 3401057 (2015).
- ⁷G.-C. Potrivitu, S. Mazouffre, L. Grimaud, and R. Jousot, *Phys. Plasmas* **26**, 113506 (2019).
- ⁸D. M. Goebel and R. M. Watkins, *Rev. Sci. Instrum.* **81**, 083504 (2010).
- ⁹A. Anders and S. Anders, *Plasma Sources Sci. Technol.* **4**, 571 (1995).
- ¹⁰S. Gershman and Y. Raitses, *J. Phys. D: Appl. Phys.* **51**, 235202 (2018).
- ¹¹J. Y. Kim, J. Y. Jang, J. Choi, J.-i. Wang, W. I. Jeong, M. A. I. Elgarhy, G. Go, K.-J. Chung, and Y. S. Hwang, *Plasma Sources Sci. Technol.* **30**, 025011 (2021).
- ¹²G. Bachet, F. Skiff, M. Dindelegan, F. Doveil, and R. A. Stern, *Phys. Rev. Lett.* **80**, 3260 (1998).
- ¹³S. Mazouffre, *Plasma Sources Sci. Technol.* **22**, 013001 (2012).
- ¹⁴C.-S. Yip and D. Jiang, *Plasma Sci. Technol.* **23**, 055501 (2021).
- ¹⁵W. B. Amos and J. G. White, *Biol. Cell* **95**, 335 (2003).
- ¹⁶P. O. Bayguinov, D. M. Oakley, C.-C. Shih, D. J. Geanon, M. S. Joens, and J. A. J. Fitzpatrick, *Curr. Protoc. Cytom.* **85**, e39 (2018).
- ¹⁷A. Nwaneshiudu, C. Kuschal, F. H. Sakamoto, R. Rox Anderson, K. Schwarzenberger, and R. C. Young, *J. Invest. Dermatol.* **132**, 1 (2012).
- ¹⁸L. A. Bahr, T. Dousset, S. Will, and A. S. Braeuer, *J. Aerosol Sci.* **126**, 143 (2018).
- ¹⁹G. Giridhar, R. R. K. N. Manepalli, and G. Apparao, in *Spectroscopic Methods for Nanomaterials Characterization*, edited by S. Thomas, R. Thomas, A. K. Zachariah, and R. K. Mishra (Elsevier, 2017), pp. 141–161.
- ²⁰S. G. Belostotskiy, R. Khandelwal, Q. Wang, V. M. Donnelly, D. J. Economou, and N. Sadeghi, *Appl. Phys. Lett.* **92**, 221507 (2008).
- ²¹R. VanDervort, D. Elliott, D. McCarren, J. McKee, M. Soderholm, S. Sears, and E. Scime, *Rev. Sci. Instrum.* **85**, 11E408 (2014).
- ²²T. Kajiwara, K. Takeda, K. Muraoka, T. Okada, M. Maeda, and M. Akazaki, *Jpn. J. Appl. Phys.* **29**, L826 (1990).
- ²³T. Kajiwara, T. Shinkawa, K. Uchino, M. Masuda, K. Muraoka, T. Okada, M. Maeda, S. Sudo, and T. Obiki, *Rev. Sci. Instrum.* **62**, 2345 (1991).
- ²⁴T. E. Steinberger, J. W. McLaughlin, T. M. Biewer, J. F. Caneses, and E. E. Scime, *Phys. Plasmas* **28**, 082501 (2021).
- ²⁵D. S. Thompson, M. F. Henriquez, E. E. Scime, and T. N. Good, *Rev. Sci. Instrum.* **88**, 103506 (2017).
- ²⁶M. F. Henriquez, D. S. Thompson, A. J. Jemiolo, and E. E. Scime, *Rev. Sci. Instrum.* **89**, 10D127 (2018).
- ²⁷D. Caron, R. John, E. E. Scime, and T. E. Steinberger, *J. Vac. Sci. Technol. A* **41**, 033001 (2023).
- ²⁸G. D. Severn, D. A. Edrich, and R. McWilliams, *Rev. Sci. Instrum.* **69**, 10 (1998).
- ²⁹T. Lunt, G. Fussmann, and O. Waldmann, *Phys. Rev. Lett.* **100**, 175004 (2008).
- ³⁰R. F. Boivin and E. E. Scime, *Rev. Sci. Instrum.* **74**, 4352 (2003).
- ³¹Y. Raitses, D. Staack, A. Smirnov, and N. J. Fisch, *Phys. Plasmas* **12**, 073507 (2005).
- ³²See <https://www.asphericon.com/en/products/axicons> for details on the principles of operation of axicons.
- ³³S. N. Khonina, N. L. Kazanskiy, P. A. Khorin, and M. A. Butt, *Sensors* **21**, 6690 (2021).
- ³⁴See <https://www.holoor.co.il/application/diffractive-axicon-application-notes/#second> for technical details.
- ³⁵W. A. Hargus, Jr. and M. A. Cappelli, *Appl. Phys. B* **72**, 961 (2001).
- ³⁶T. Breen, N. Basque-Giroux, U. Fuchs, and I. Golub, *Appl. Opt.* **59**, 4744 (2020).
- ³⁷See <https://www.mathworks.com/matlabcentral/fileexchange/60644-deconvolution-of-two-discrete-time-signals-in-frequency-domain> for details on deconvolution algorithm.